

RF-free driving of nuclear spins with color centers in silicon carbide

Raphael Wörnle ^{1,2,3}, Jonathan Körber ^{1,2}, Timo Steidl ^{1,2}, Georgy V. Astakhov ⁴, Durga B. R. Dasari ^{1,2}, Florian Kaiser ^{5,6}, Vadim Vorobyov ^{1,2}, and Jörg Wrachtrup ^{1,2,3}

¹ 3rd Institute of Physics, University of Stuttgart, Allmandring 13, 70569 Stuttgart, Germany.

² Center for Integrated Quantum Science and Technology, 70569 Stuttgart, Germany.

³ Max Planck Institute for Solid State Research, Heisenbergstraße 1, 70569 Stuttgart, Germany.

⁴ Helmholtz-Zentrum Dresden-Rossendorf, Institute of Ion Beam Physics and Materials Research, 01328 Dresden, Germany.

⁵ Quantum Materials, Luxembourg Institute of Science and Technology (LIST), 28 Avenue des Hauts Fourneaux, 4362 Belval, Luxembourg.

⁶ University of Luxembourg, 2 Avenue de l'Université, 4365 Belval, Luxembourg.

Abstract

Color centers that enable nuclear-spin control without RF fields offer a powerful route towards simplified and scalable quantum devices. Such capabilities are especially valuable for quantum sensing and computing platforms that already find applications in biology, materials science, and geophysics. A key challenge is the coherent manipulation of nearby nuclear spins, which serve as quantum memories and auxiliary qubits but conventionally require additional high-power RF fields which increase the experimental complexity and overall power consumption. Finding systems where both electron and nuclear spins can be controlled using a single MW source is therefore highly desirable. Here, using a modified divacancy center in silicon carbide, we show that coherent control of a coupled nuclear spin is possible without any RF fields. Instead, MW pulses driving the electron spin also manipulate the nuclear spin through hyperfine-enhanced effects, activated by a precisely tilted external magnetic field. We demonstrate high-fidelity nuclear-spin control, achieving 89% two-qubit tomography fidelity and nearly T_1 -limited nuclear coherence times. This approach offers a simplified and scalable route for future quantum applications.

INTRODUCTION

4H-silicon carbide (SiC) has recently emerged as a promising platform to host point defects with possible applications in quantum technologies, such as distributed quantum computing or sensing [1, 2].

SiC contains a multitude of different color centers [3, 4]. One of the most studied color center is the silicon vacancy center (V_{Si}), in particular the so-called V2 center is a promising candidate in the field of quantum communication due to its encouraging properties at low temperatures (LT) [5–7]. Other widely researched color centers are divacancies ($V_{Si}V_C$), the so-called PL1-4 centers (named after their four possible orientations within the 4H-SiC lattice) [8–10]. These defects have also achieved excellent results at cryogenic temperatures reaching seconds-long spin coherence times [11, 12], as well as lifetime-limited optical linewidths [13–15], both being essential for quantum communication and distributed quantum computing. Current research investigates how to integrate these color centers into photonic (nano-)structures to maximize count rates, and thus application relevance [5, 16, 17].

Quite recently, a new family of color centers, modified divacancies in SiC, was discovered [18, 19]. The current understanding of those modified divacancies is related to a nearby antisite which suggests, that a reliable implantation and creation of those color centers is possible. This interpretation is supported by recent theoretical works proposing the correspondence of a divacancy coupled to a nearby

carbon antisite at different crystallographic positions [20, 21].

Out of those modified divacancy centers the so-called PL6 centers demonstrate with their high count rate from bulk emitters (~ 200 kcps) and high spin readout contrast ($\sim 30\%$) at room temperature [18], that they can match the performance of the long-studied NV center in diamond [22–24], making them suitable candidates for potential room temperature sensing applications. For PL6 centers, further improvements to 60 % spin readout contrast already were demonstrated in highly strained SiC membranes [25]. Additionally, quantum technologies based on modified divacancies in SiC offer a pathway towards full CMOS compatibility and wafer-scale fabrication [26, 27]. Besides this, modified divacancies such as the PL6 center are potentially well-suited for biology studies, considering their emission spectrum in the second biological window (1000 - 1300 nm) due to reduced scattering and absorption in tissue [8].

Recent progress has also been made on integrating PL6 centers into nanophotonic structures to further improve their count rates [28–30], and first cryogenic optical studies have been performed to probe their optical properties in more detail [31].

Due to their aforementioned favorable optical and spin properties, PL6 centers also enable sensing and control of nearby nuclear spins. Nuclear spins in the local environment couple to the electron spin of the defect, allowing them to be detected and used as qubit registers for quantum information storage. Conventionally, nuclear-spin

^{*} raphael.woernle@pi3.uni-stuttgart.de

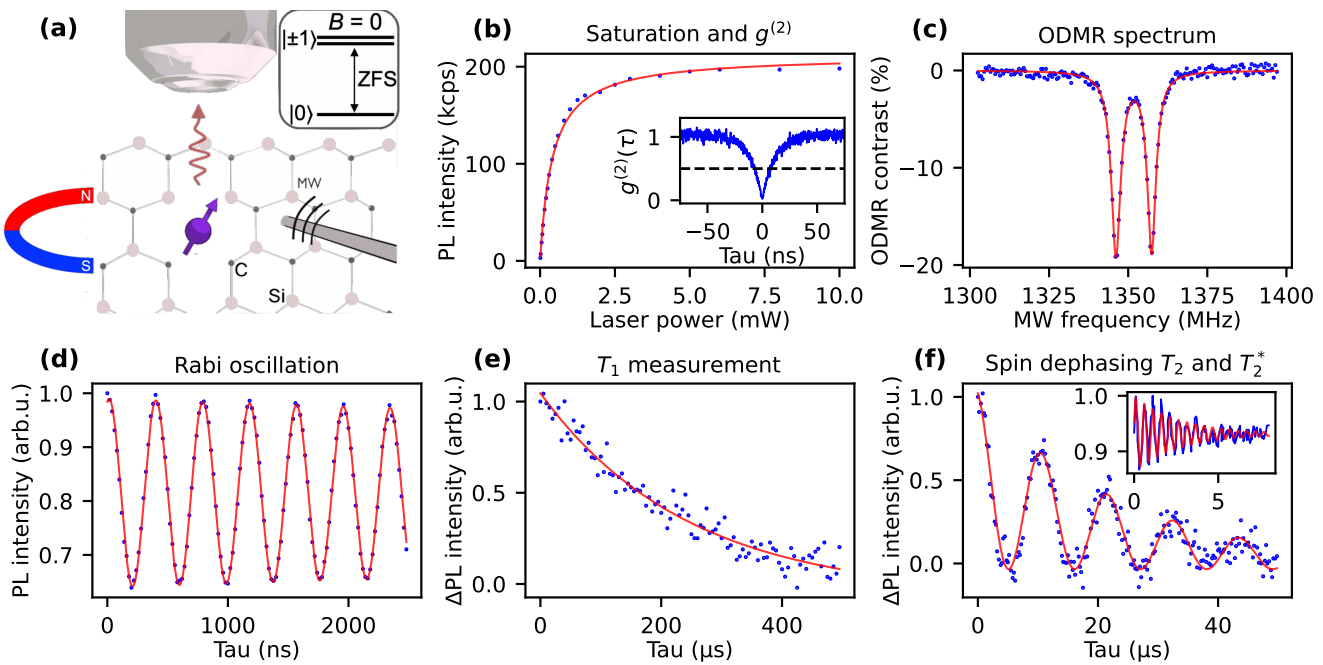


Figure 1: Properties of a single PL6 center. (a) Schematic representation of a PL6 center with ground state level structure and the experimental apparatus with wire for MW, and external magnetic field and objective for excitation and collection of the fluorescence emission. (b) Saturation study of a single PL6 center with a saturation intensity of 211.7 ± 1.8 kcps. Inset shows the second order correlation function $g^{(2)}(\tau)$ confirming a clear single defect behavior. (c) CW-ODMR spectrum of a single PL6 center in zero magnetic field with a two-Lorentzian fit function centered around 1351.8 MHz. (d) Rabi oscillation fitted with a damped cosine function. (e) Measurement of the spin-lattice relaxation time T_1 in a magnetic field of $B = 210$ G. A single exponential fitting function was used to determine $T_1 = 242.8 \pm 22.1$ μ s. (f) Hahn echo measured in a magnetic field of $B = 210$ G. T_2 is estimated from the damped cosine fitting to $T_2 = 25.0 \pm 1.3$ μ s. Inset shows Ramsey measurement measured at a detuning of 3 MHz yielding a pure spin-dephasing time $T_2^* = 2.7 \pm 0.3$ μ s.

manipulation requires strong radio-frequency (RF) pulses because of their weak magnetic moment. Eliminating RF fields in favor of weaker microwave (MW) pulses is therefore highly advantageous, reducing experimental complexity and power consumption, avoiding RF-induced heating, and minimizing thermal drift — particularly relevant in low-temperature measurements.

In this work, we demonstrate RF-free nuclear spin control enabled by precisely tilting the externally applied magnetic field, which activates hyperfine-mediated nuclear spin precession. The observed nuclear spin precession further provides a sensitive probe of the magnetic-field orientation, enabling accurate field alignment using the coupled nuclear spin itself.

RESULTS AND DISCUSSION

Spin properties of PL6 centers

Figure 1a illustrates a schematic representation of the measurement apparatus with a PL6 center. A power-dependent saturation study on a single PL6 center, depicted in Figure 1b, yields a background-corrected saturation count rate of $I_S = 211.7 \pm 1.8$ kcps, consistent with previously reported values for unstructured bulk samples [18]. Autocorrelation measurements using a Hanbury-

Brown and Twiss interferometer confirm with $g^{(2)}(0) \ll 0.5$ that the signal originates from a single defect center, depicted in the inset in Figure 1b and in Supplementary Figure S1. In this work, individual PL6 centers are identified by their characteristic zero-field splitting (ZFS) measured through continuous-wave optically detected magnetic resonance (CW-ODMR) measurements. Figure 1c shows a typical CW-ODMR spectrum of a single PL6 center recorded at a laser power of 50 μ W in zero magnetic field, exhibiting its two characteristic ODMR dips. The data are fitted with a double Lorentzian function, yielding $f_1 = 1346.1$ MHz and $f_2 = 1357.4$ MHz, corresponding to the $m_s = 0 \rightarrow m_s = \pm 1$ transitions, with a measured contrast of approximately 19 %. This results in ZFS parameters $D = 1351.8$ MHz and $E = 5.6$ MHz which are in good agreement with previous reports of PL6 centers [8, 10, 18, 32].

Using pulsed measurements, the spin readout contrast can be enhanced even more. Here, Rabi oscillation measurements show a contrast of 35 %, fitted with a damped cosine function, as shown in Figure 1d.

The spin coherence times, critical for quantum technology applications, were characterized at an applied magnetic field of 210 G to suppress spin-bath decoherence. The spin-lattice relaxation time T_1 was determined to be

$242.8 \pm 22.1 \mu\text{s}$, while the spin-spin relaxation time T_2 was measured to be $25.0 \pm 1.3 \mu\text{s}$, as shown in Figure 1e. The inhomogeneous spin-dephasing time T_2^* is deduced to be $2.7 \pm 0.3 \mu\text{s}$, displayed in the inset of Figure 1e. While the relaxation times T_2 and T_2^* are comparable to previous reports, the measured T_1 is nearly twice as long as previously reported values at room temperature [18, 28]. The improved relaxation times are attributed, in part, to the use of a higher intrinsic quality of our sample.

Coherent control of single nuclear spins

Unlike diamond, SiC has the advantage of having a diatomic base consisting of silicon and carbon atoms. This means that it has more stable isotopes with a non-zero nuclear spin than diamond: ^{13}C with a natural abundance of 1.1 % and ^{29}Si with 4.7 %, respectively. We found one PL6 center strongly coupled to a nearby nuclear spin with a coupling strength of 6.7 MHz (Supplementary Figures S1, S2 & S3). A schematic representation of the coupling of the PL6 center with the nuclear spin is shown in Figure 2a. The characteristic CW-ODMR splitting can be seen in Figure 2b without and with increasing external magnetic field. In contrast to an ODMR spectrum without coupled nuclear spins, the $m_s = \pm 1$ transitions are additionally split by the hyperfine interaction with the nuclear spin. Inspired by Hu et al. [28], we performed Rabi oscillations on the nuclear spin using the sequence depicted in Figure 2c.

The experimental result is illustrated in green in Figure 2e. The precession can be observed without the need for an additional RF source. First, we initialize the nuclear spin with a short laser pulse, after which we apply a spin-selective π pulse on the electron spin (here, on the $| -1, \uparrow \rangle$) transition after which a waiting time as well as another π pulse are applied before readout. It results in a much slower oscillation compared to the electron Rabi oscillations. Additionally, it becomes evident that the Rabi oscillation of the nuclear spin decays much slower than the Rabi measurement of the electron spin shown in Figure 1d.

This can be explained as follows: in contrast to manipulating electron spins, which is achieved through optical excitation and the application of microwave signals, manipulating nuclear spins additionally requires the ability to control the nuclear spin via the electron spin. When the electron spin is initialized by a laser pulse, the nuclear spin is in a mixed state of spin up and spin down. To polarize the nuclear spin, the nuclear spin is first mapped onto the electron spin by applying a microwave π pulse, and then the electron spin is reinitialized by a short laser pulse [33]. This results in the nuclear spin being polarized and the contrast being increased even further (Supplementary Figure S4). It is important that the laser polarization pulse after $T_{\text{Larmor}} = \omega_{\text{nuc}}/\pi$ is applied after the π pulse to achieve maximum polarization. This is shown in blue in Figure 2e. Since a similar control is achieved as in the previous work by Hu et al., but in a different measurement configuration without the application of an RF pulse, a more detailed investigation is required here.

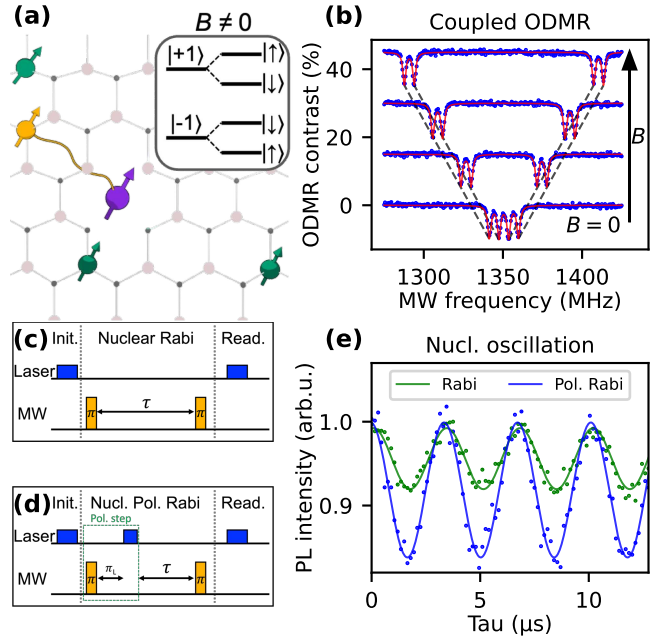


Figure 2: PL6 coupled to nearby nuclear spin. (a) Schematic representation of a single color center coupled to a nearby nuclear spin and a coupling strength of 6.7 MHz with shown hyperfine splitting. (b) ODMR spectra of the coupled PL6 center spin without and with applied magnetic field up to a field strength of 20 G and corresponding Zeeman splitting. (c) Pulse sequence for nuclear oscillation. The $| -1, \uparrow \rangle$ transition from the ODMR measurement is used as a frequency for the MW pulse. (d) Modified version of the pulse sequence shown in (c) with laser polarization step to further polarize the nuclear spin. (e) Experimental results measured at an external magnetic field of 240 G for the shown pulse sequences without (green) and with (blue) polarized oscillation with corresponding fit functions.

Model

The Hamiltonian of the system can, in general, be written as

$$H = DS_z^2 + E (S_x^2 - S_y^2) + \gamma_e \mu_B \mathbf{B} \cdot \mathbf{S} + \mathbf{S} \cdot \mathbf{A} \cdot \mathbf{I} - \gamma_N \mathbf{I} \cdot \mathbf{B}. \quad (1)$$

where the experimentally determined axial zero-field splitting and the transverse (non-axial) component are given by D and E , respectively. \mathbf{S} and \mathbf{I} denote the electron and nuclear spin operators, \mathbf{A} is the hyperfine interaction tensor, and \mathbf{B} is the externally applied magnetic field. The external magnetic field can be decomposed into components parallel and perpendicular to the quantization axis as shown in Figure 3a.

Analogous to Bürgler et al. [34], the effective Hamiltonian can now be determined using Van Vleck perturbation theory for the $m_s = 0$ ground-state subspace $\{| 0, -1/2 \rangle, | 0, +1/2 \rangle\}$ (The full derivation of the effective Hamiltonian is given in the Supplementary information). In this treatment, the transverse component of the zero-field splitting is neglected because $E \ll D$, so that it yields only

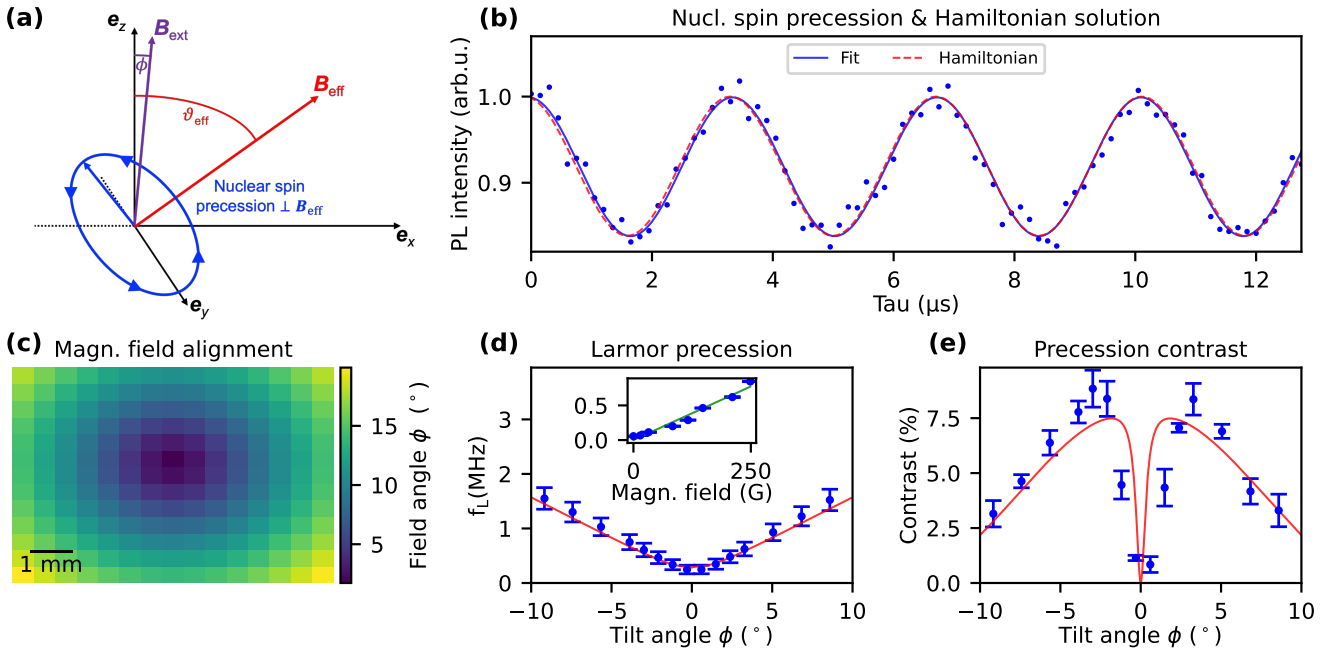


Figure 3: Theoretical derivation of nuclear oscillation. (a) Schematic representation of the tilt of the magnetic field causing the precession of the nuclear spin with enhanced oscillation amplitude due to gyromagnetic enhancement. (b) Nuclear oscillation experimental data (blue) & fit function (blue line) with derived theoretical solution of the Hamiltonian (red dashed line) at an external magnetic field of 240 G and a tilt angle $\phi = 2^\circ$. (c) Field angle ϕ calculated from experimental data for different planar alignments of the magnetic field. (d) Larmor frequency in dependence of the tilt angle ϕ of the magnetic field with theoretical data of the Hamiltonian. Inset shows the Larmor frequency of the nuclear oscillation in dependence of the external magnetic field strength with linear fit function $f_L \propto B$. (e) Contrast of the nuclear oscillation in dependence of the magnetic tilt angle ϕ in comparison to the theoretical values.

a small energetic offset and does not significantly mix the electron-spin manifolds. The remaining corrections arise from virtual transitions to the $m_s = \pm 1$ states induced by the transverse hyperfine interaction. This leads to the following effective Hamiltonian:

$$H_{\text{eff}} = \frac{1}{2} \begin{pmatrix} \gamma_l B_z + \nu_z & \gamma_l B_\perp + \nu_\perp \\ \gamma_l B_\perp + \nu_\perp & -\gamma_l B_z - \nu_z \end{pmatrix}, \quad (2)$$

where the correction terms

$$\nu_z = \frac{\gamma_e B_z A_\perp^2}{D^2 - (\gamma_e B_z)^2}, \quad \nu_\perp = -\frac{2\gamma_e B_\perp A_\perp D}{D^2 - (\gamma_e B_z)^2} \quad (3)$$

represent second-order shifts of the diagonal and off-diagonal matrix elements, respectively. These terms originate from the mixing between the $m_s = 0$ and $m_s = \pm 1$ manifolds and therefore depend on the transverse hyperfine coupling A_\perp as well as the tilt of the external magnetic field parameterized by $B_\perp = B \sin \phi$ (Figure 3a).

Diagonalizing Eq. (2) yields the nuclear precession frequency

$$f_{\text{nuc}} = \gamma_l |\mathbf{B}_{\text{eff}}| = \sqrt{(\gamma_l B_z + \nu_z)^2 + (\gamma_l B_\perp + \nu_\perp)^2}, \quad (4)$$

as well as the tilt angle of the effective magnetic field,

$$\vartheta_{\text{eff}} = \tan^{-1} \left(\frac{\gamma_l B_\perp + \nu_\perp}{\gamma_l B_z + \nu_z} \right). \quad (5)$$

The transverse component of the magnetic field plays a central role in this dynamics: the term $\gamma_l B_\perp$ drives nuclear mixing directly, while the electron-mediated correction ν_\perp enhances this effect for larger A_\perp and reduces it for stronger applied magnetic fields. In contrast, the diagonal correction ν_z modifies the effective nuclear Zeeman splitting. In the special case of a perfectly aligned magnetic field ($B_\perp = 0$) and a purely axial hyperfine tensor ($A_\perp = 0$), both correction terms vanish. The Hamiltonian becomes diagonal, and consequently no nuclear precession is observed.

Additionally, one can determine the contrast C of the nuclear precession. While the ideal contrast of the nuclear spin oscillation is determined by the relative strength of the perpendicular ($\gamma_l B_\perp + \nu_\perp$) and parallel ($\gamma_l B_z + \nu_z$) fields, one must also account for the readout contrast of the electron spin, which degrades in the presence of a perpendicular field B_\perp . Using a simple two-level model for the electron, the final contrast of the nuclear spin oscillation can be written as

$$C = C_e(\phi) \circ C_n(\phi) = C_e(\phi) \circ \left(\frac{\gamma_l B_\perp + \nu_\perp}{f_{\text{nuc}}} \right)^2. \quad (6)$$

The total observable nuclear spin contrast C_n is convoluted with the electronic readout contrast (C_e) which decreases with increasing B_\perp . Within the two-level approximation this contrast can be simply written as $C_e \sim \left(\frac{\gamma_e B_z - A_{||}}{f_e} \right)^2$,

where the detuned electron spin precision frequency $f_e = \sqrt{(\gamma_e B_z - A_{\parallel})^2 + (\gamma_e B_{\perp})^2}$.

The relation between the different orientations of the external and effective magnetic field, the defect orientation and the nuclear spin precession is shown schematically in Figure 3a. The external magnetic field is slightly tilted relative to the crystal axis. This tilt causes the effective magnetic field to be strongly tilted relative to the external magnetic field. This leads to the precession of the nuclear spin observed in Figure 2e. Substituting the experimental values for the measured precession of the nuclear spin in Figure 2e yields the Hamiltonian solution, which is shown in Figure 3b with the experimental results and the fit function. It can be seen that the theoretical values are in very good agreement with the experimental ones. In this case, a magnetic tilt of $\phi = 2^\circ$ was determined for the defect with the hyperfine couplings of $A_z = 6.7$ MHz and $A_{\perp} = 5.5$ MHz.

Magnetic field alignment

Precise alignment of the external magnetic field relative to the defect axis is crucial for both electron and nuclear spin control. Several established methods exist, including alignment via ODMR transitions, analysis of the spin Hamiltonian, or monitoring the fluorescence count rate of the color center [35] (Supplementary Figure S5). The alignment of the field using the spin Hamiltonian is shown as an example in more detail in Figure 3c. In this work, we demonstrate that nuclear spin precession provides a complementary and sensitive method to determine the field orientation.

The nuclear spin precession frequency and the observable contrast of its oscillations are strongly dependent on the tilt angle ϕ of the external field relative to the defect axis. As derived from the effective Hamiltonian, the precession frequency is primarily determined by the longitudinal component of the effective field, $f_{\text{nuc}} \sim \gamma_1 B_z + \nu_z$, with small quadratic corrections from the transverse component ν_{\perp} . In contrast, the oscillation amplitude (contrast) scales linearly with the transverse component, $C_n \propto (\gamma_1 B_{\perp} + \nu_{\perp})^2$, while simultaneously being modulated by the electron spin readout, which decreases for increasing B_{\perp} (see Eq. 6). Consequently, nuclear spin precession and electron readout contrast exhibit opposing dependencies on the perpendicular field component.

Experimentally, this interplay results in a “sweet spot” for magnetic field alignment: a small, finite tilt of the external field maximizes the nuclear spin contrast, while keeping the oscillation frequency moderate, as illustrated in Figures 3d and 3e. At zero tilt, the nuclear spin sees only a longitudinal field and the precession contrast vanishes, even though the Larmor frequency f_0 remains finite. As the tilt increases, the precession amplitude grows linearly with ϕ , but the electron readout contrast decreases due to misalignment of the electron spin eigenstates. By fitting the experimentally measured nuclear precession fre-

quency and contrast to the theoretical model, we extract both the tilt angle $\phi \sim 2^\circ$ and the hyperfine couplings $A_z = 6.7$ MHz and $A_{\perp} = 5.5$ MHz, demonstrating excellent agreement between theory and experiment.

For practical applications, a further consideration arises from the trade-off between oscillation speed and signal-to-noise ratio (SNR). Faster nuclear precession allows more operations to be performed within the nuclear coherence time $T_2^{*,\text{Nuc}}$, which is advantageous for quantum control and sensing. However, faster precession typically requires a larger transverse effective field, which, as discussed, reduces the electron readout contrast, and thereby the observed nuclear oscillation amplitude and SNR. Consequently, the experimental protocol must balance a sufficiently fast precession for timely operations with a large enough contrast to ensure high-fidelity readout. The sweet spot for nuclear spin contrast naturally accounts for this trade-off, providing an optimal tilt that maximizes the observable oscillation amplitude without excessively compromising the electron spin readout.

Nuclear spin relaxation and coherence times We further demonstrate the application of the nuclear spin as a quantum memory. By transferring the electron-spin state onto the nuclear spin, the observed signal decays dramatically more slowly than the corresponding electron-spin coherence, highlighting a substantially longer nuclear coherence time. The spin decoherence time $T_2^{*,\text{Nuc}}$ is of particular interest here, as it is a well known measure to determine the magnetic sensitivity, an important quantitative criterion benchmark for potential applications in quantum sensing and metrology. The sensitivity can be determined quantitatively via the spin decoherence time to $\eta \propto 1/T_2^{*}$ [36]. Here, the pure dephasing time of the nuclear spin can be determined. Therefore, the sequence from Figure 2d gets modified in a way that both microwave transitions $|1, \uparrow\rangle$ and $| -1, \uparrow\rangle$ are applied at the same time for driving the nuclear spin. The corresponding sequence is illustrated in Figure 4a. The measurement with a damped cosine fit function is depicted in Figure 4c and results in a spin decoherence time $T_2^{*,\text{Nuc}} = 102.2 \pm 7.2 \mu\text{s}$. Compared to the electron spin, the nuclear spin has a T_2^* that in this case is more than 30 times longer, a significant improvement for the magnetic sensitivity.

To access the nuclear-spin coherence, the pulse sequence in Figure 4a is modified by inserting two fast π pulses on the selected ODMR transition, separated by a time interval corresponding to the hyperfine splitting, i.e. $\Delta t = \pi/\omega_1$ with $\omega_1 = 2\pi \cdot 6.7$ MHz. The resulting sequence is shown in Figure 4b. Experimentally, this produces a pronounced nuclear-spin echo whose decay time exceeds that of the electron spin. As shown in Figure 4d, the signal is well described by a damped squared-cosine fit, yielding a nuclear-spin relaxation time of $T_2^{\text{Nuc}} = 151.0 \pm 6.9 \mu\text{s}$, approximately six times longer than the electron-spin T_2 . This extended coherence is consistent with the nuclear-spin dynamics being limited by the electron-spin T_1 , an ef-

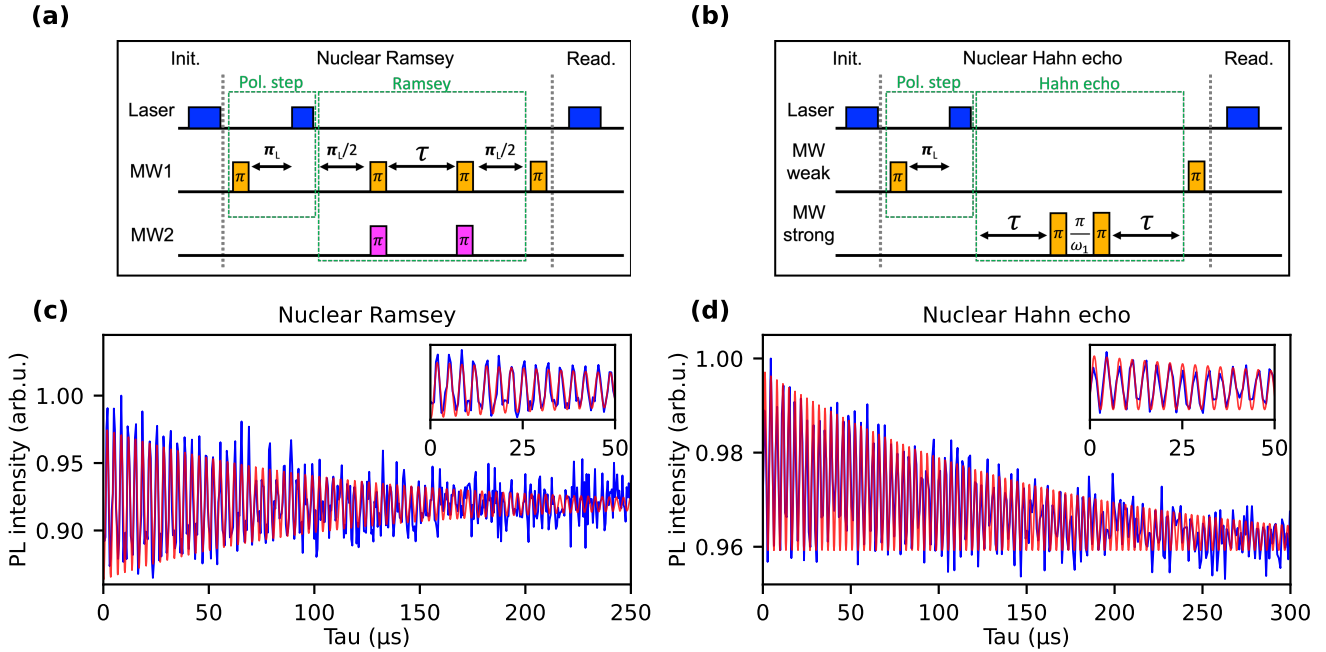


Figure 4: Nuclear Ramsey and spin echo. (a) & (b) Schematic pulse sequence for the Ramsey ($T_2^{*,\text{Nucl}}$) and nuclear spin echo (T_2^{Nucl}) measurement. For the Ramsey measurement, both microwave transitions $|1, \uparrow\rangle$ and $| -1, \uparrow\rangle$ are applied at the same time for driving the nuclear spin. For the nuclear spin echo measurement, two "fast" π pulses are applied for Hahn echo, as first performed by Dutt et al. [33]. (c) & (d) Experimental result for the Ramsey and nuclear spin echo measurement yielding a spin dephasing time $T_2^{*,\text{Nucl}} = 102.2 \pm 7.2 \mu\text{s}$ and a spin echo time for the nuclear spin of $T_2^{\text{Nucl}} = 151.0 \pm 6.9 \mu\text{s}$. Each inset shows a zoomed in version of the first 50 μs .

fect previously reported for NV centers in diamond [34, 37, 38].

Quantum state tomography (QST) under a tilted effective field

Finally, we explore whether the method presented allows for a full set of quantum operations, sufficient, e.g., to perform quantum state tomography. Earlier, the nuclear spin Hamiltonian in the presence of a tilted magnetic field always contains a non-zero longitudinal component, $H_{\text{eff}} = \frac{1}{2}(\Omega_z\sigma_z + \Omega_x\sigma_x)$, with $\Omega_z = \gamma_1 B_z + \nu_z$ and $\Omega_x = \gamma_1 B_{\perp} + \nu_{\perp}$. As a result, the Bloch sphere is not fully accessible: starting from $|0\rangle$, the spin states after nominal $\pi/2$ and π pulses are now given by

$$|\psi_{\pi/2}\rangle = \frac{1}{\sqrt{2}} \left[(1 - i \cos \vartheta_{\text{eff}}) |0\rangle - i \sin \vartheta_{\text{eff}} |1\rangle \right], \quad (7)$$

$$|\psi_{\pi}\rangle = -i \left[\cos \vartheta_{\text{eff}} |0\rangle + \sin \vartheta_{\text{eff}} |1\rangle \right], \quad (8)$$

with $\vartheta_{\text{eff}} = \tan^{-1}(\Omega_x/\Omega_z)$. In such conditions, preparing ideal superposition states and performing ideal single qubit gates such as the Hadamard gate is challenging.

Despite these limitations, state tomography is still possible. By applying pulses along the available tilted axis and performing projective measurements in the computational basis, one can obtain expectation values along three non-collinear axes in the XZ -plane i.e., $\hat{n}_1 = (0, 0, 1)$, $\hat{n}_2 = (\sin 2\theta_{\text{eff}}, 0, \cos 2\theta_{\text{eff}})$, $\hat{n}_3 = (\sin \theta_{\text{eff}}, 0, \cos \theta_{\text{eff}})$. These measurements allow reconstruction of the nuclear Bloch

vector in the XZ -plane with unit fidelity. The Y -components can be accessed only indirectly by accessing the other electronic state, wherein the nuclear spin has only a phase evolution due to the additional detuning caused by A_{\parallel} (Supplementary Information). Together with such an additional phase gate we will be able to process a general one qubit QST. In the following, we experimentally showcase this for some special cases and give the more detailed analysis in the Supplementary Information.

First, we show a one-qubit gate for the electron and nuclear spin individually, depicted in Figures 5 a and b, respectively. From the corresponding reconstructed density matrices, a fidelity of 97 % can be determined for the electron spin and 93 % for the nuclear spin, showing high individual control over both single spins. Finally, a maximally entangled state, a Bell state $|\Psi^+\rangle = (|0, \uparrow\rangle + |1, \downarrow\rangle)/\sqrt{2}$ is generated by applying two additional gates, shown in Figure 5c. The corresponding quantum operations are used as a combination of the MW pulses and waiting times already used in the one-qubit gates. In both cases, the Z -component can be read out straight forward without any additional sequences. For the electron spin manipulation, a MW phase shifter is used to apply 90 ° MW pulses in the X - and Y -plane. For the nuclear spin, the X -component can be manipulated by applying a waiting time corresponding to a 90 ° rotation. As mentioned before, the Y -component is accessed through applying two MW π pulses to generate a Phase onto the nuclear spin with a subsequent 90 ° rotation waiting time. By combin-

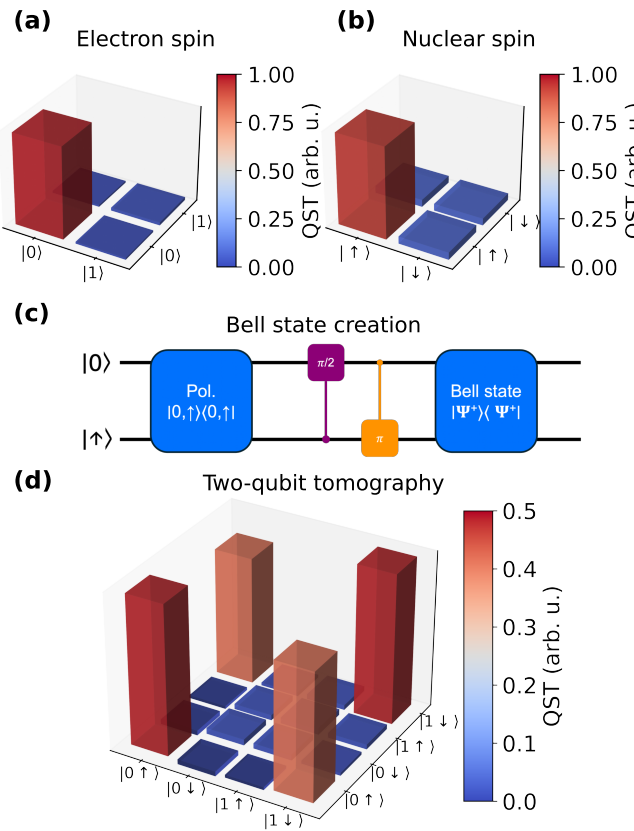


Figure 5: Quantum state tomography. Single qubit tomography for the electron spin **(a)** and the nuclear spin **(b)** with reconstructed density matrix shown and a corresponding gate fidelity of 97 % and 93 %, respectively. **(c)** Schematic representation of entanglement generation. A global $\pi/2$ MW pulse on the electron spin and a subsequent π pulse applied as a waiting time are used to create the Bell state from the polarized initial state. **(d)** Two-qubit tomography for the nuclear spin coupled PL6 center yielding a fidelity of 89 %.

ing each three gate operations for the electron spin with the three nuclear spin gate operations, the two-qubit tomography can be performed. The resulting density matrix is shown in Figure 5d. Here, also, a fidelity of 89 % can be determined yielding a similar result to that of Hu et al. [28], which shows a high coherent control of the entangled state through the driving of the nuclear spin but without any external RF-signal. The corresponding data as well as the detailed measurement sequences of the quantum state tomography are presented in the Supplementary Figures S6, S7 & S8.

Summary and Outlook

In conclusion, we have demonstrated coherent control of a nuclear spin in SiC at room temperature by utilizing a strongly coupled PL6 center without the necessity of a direct, RF-assisted driving of the nuclear spin. The high fidelity control of the nuclear spin is enabled by using its precession in a precisely tilted magnetic field, combined with

the coherent control of the electron spin of a strongly coupled PL6 center, that is used for initialization and read out. Here, the high photon count rate and high spin readout contrast of the PL6 center at room temperature are key to our results. Additionally, state-of-the-art gate fidelities are achieved for a one- and two-qubit tomography reaching 97 % for a single qubit gate and 89 % for the two-qubit tomography. Furthermore, we showed that we can also use the nuclear spin as storage, thus achieving more extensive information storage than with the rapidly decohering electron spin of a single PL6 center. Here, a nearly T_1 -limited nuclear spin coherence time of $T_2^{\text{Nuc}} = 151.0 \pm 6.9 \mu\text{s}$ is achieved, being a factor of 6 higher compared to the electron spin coherence time. This method should also be easily extendable to the coupling of multiple nuclear spins, thus paving the way for the scalable development of defects in SiC for room temperature quantum applications.

Methods

Sample fabrication The sample of this study is a natural abundance SiC wafer with a 10 μm -thick grown epi-layer (TySiC) with a doping concentration of $[N] = 8.13 \cdot 10^{15} \text{ cm}^{-3}$. Nitrogen ions were implanted at 30 keV with a dose of $2.5 \cdot 10^{11} \text{ ions/cm}^2$ to create the PL6 color centers. Simulations show a depth of defects of approximately 50 nm below the surface [39]. After the ion implantation, the sample was subjected to a two-step annealing process in a vacuum ($p < 10^{-6} \text{ mbar}$), first for two hours at 500 $^{\circ}\text{C}$ and then for one hour at 900 $^{\circ}\text{C}$.

Optical characterization and spin manipulation All measurements were performed at room temperature. For the measurements, a home-built confocal microscopy setup is used. A 940 nm laser (Thorlabs, M9-940-0200) was used for excitation, and the fluorescence was collected with single-photon detectors (SNSPDs, Photon Spot). The fluorescence emitted by the defects was filtered from the excitation light using a 1000 nm longpass dichroic filter and then further filtered through a 1000 nm longpass filter. The excitation laser is pulsed with an acousto-optical modulator (AOM EQ Photonic 3200-124). In all experiments, a 50 μm thick copper wire is placed on the sample in close proximity to the implanted areas. The microwave signals are generated through vector signal generators (SMIQ03B & SML03, Rhode & Schwarz) and pass through multiple switches (ZASWA-2-50DR+, Mini Circuits) and a subsequent amplifier (ZHL-25W-272+, Mini Circuits) via SMA cables onto the wire attached to the sample. 90 degree phase shifters (ZX10Q-2-34-S+, Mini Circuits) are used for phase control of the spins. A permanent neodymium magnet was used to generate an external magnetic field. This magnet was mounted on a stage with three linear translation stages (Thorlabs) to enable a precise and reproducible movement of the magnet in all three dimensions. Additionally, a single PL6 center was used to calculate the magnetic field strength using ODMR measurements.

DATA AVAILABILITY

The data supporting the presented findings are available at the following repository: [Linktobecreated](#).

CODE AVAILABILITY

The measurement and evaluation codes used for this study are available from the corresponding author upon reasonable request.

COMPETING INTERESTS

The authors declare no conflict of interest.

ACKNOWLEDGEMENTS

We acknowledge fruitful discussions and experimental help from Erik Hesselmeier-Hüttmann, Rouven Maier, Marcel Krumrein, Adil Dogan, Rainer Stöhr and Pierre Kuna. Furthermore, we thank Arnold Weible from the Max Planck Institute for Intelligent Systems for helping with the first attempts of the annealing procedure.

This research was supported by the German Federal Ministry of Research, Technology and Space via the project QVOL2 (Grant agreement No. 03ZU2110GB) as well as the project QSi2V (Grant agreement No. 13N16756). The project received funding from the European Union's Horizon Europe research and innovation program through the SPINUS project (Grant agreement No. 101135699). This research was supported by the European Commission via the project C-QuEnS (Grant Agreement No. 101135359). G.V.A. acknowledges the project Quantum Sensing for Fundamental Physics (QS4Physics) from the Innovation pool of the research field Helmholtz Matter of the Helmholtz Association as well as the IBC facilities at the HZDR for support. F.K. acknowledges support by the Luxembourg National Research Fund (FNR) via the PEARL chair "AQuaTSiC" under grant agreement 17792569 as well as the project "SiCqurTech" under grant agreement 18253399. F.K. additionally acknowledges the European Research Council for the project "Q-Chip" under grant agreement 101171067, the European Union's Horizon 2020 Research and Innovation Programme via the QuantERA project "SiCqurTech" under grant agreement 101017733, and the Horizon Europe Programme for the Flagship project "QIA" under grant agreement 101102140.

AUTHOR CONTRIBUTIONS

The project was conceived by R.W. and J.W. and supervised by F.K., D.D., V.V. and J.W. R.W. and J.K. prepared the samples and performed the annealing. R.W and G.V.A designed the ion implantation. R.W., J.K., T.S. and F.K. designed and constructed the optical setup. The optical measurements were conducted by R.W. and analyzed by R.W., D.D. and J.W. D.D. performed the simulations. The manuscript was written by R.W., J.K., D.D., V.V. and F.K. All authors contributed to the manuscript.

References

1. Zhou, Y. *et al.* Silicon carbide: A promising platform for scalable quantum networks. *Applied Physics Reviews* **12**, 031301 (2025).
2. Castelletto, S. *et al.* Silicon Carbide Photonics Bridging Quantum Technology. *ACS Photonics* **9**, 1434–1457 (2022).
3. Son, N. T. *et al.* Developing silicon carbide for quantum spintronics. *Applied Physics Letters* **116**, 190501 (2020).
4. Castelletto, S. & Boretti, A. Silicon carbide color centers for quantum applications. *JPhys Photonics* **2**, 022001 (2020).
5. Babin, C. *et al.* Fabrication and nanophotonic waveguide integration of silicon carbide colour centres with preserved spin-optical coherence. *Nature Materials* **21**, 67–73 (2022).
6. Morioka, N. *et al.* Spin-controlled generation of indistinguishable and distinguishable photons from silicon vacancy centres in silicon carbide. *Nature Communications* **11**, 2516 (2020).
7. Simin, D. *et al.* Locking of electron spin coherence above 20 ms in natural silicon carbide. *Physical Review B* **95**, 161201(R) (2017).
8. Koehl, W. F., Buckley, B. B., Heremans, F. J., Calusine, G. & Awschalom, D. D. Room temperature coherent control of defect spin qubits in silicon carbide. *Nature* **479**, 84–87 (2011).
9. Christle, D. J. *et al.* Isolated spin qubits in SiC with a high-fidelity infrared spin-to-photon interface. *Physical Review X* **7**, 021046 (2017).
10. Falk, A. L. *et al.* Polytype control of spin qubits in silicon carbide. *Nature Communications* **4**, 1819 (2013).
11. Anderson, C. P. *et al.* Five-second coherence of a single spin with single-shot readout in silicon carbide. *Sci. Adv.* **8**, 5912 (2022).
12. Christle, D. J. *et al.* Isolated electron spins in silicon carbide with millisecond coherence times. *Nature Materials* **14**, 160–163 (2015).
13. Udvarhelyi, P. *et al.* Vibronic States and Their Effect on the Temperature and Strain Dependence of Silicon-Vacancy Qubits in 4H-SiC. *Physical Review Applied* **13**, 054017 (2020).
14. Steidl, T. *et al.* Single V2 defect in 4H silicon carbide Schottky diode at low temperature. *Nature Communications* **16**, 4669 (2025).
15. Anderson, C. P. *et al.* Electrical and optical control of single spins integrated in scalable semiconductor devices. *Science* **366**, 1225–1230 (2019).
16. Krumrein, M. *et al.* Precise Characterization of a Waveguide Fiber Interface in Silicon Carbide. *ACS Photonics* **11**, 2160–2170 (2024).

17. Körber, J. *et al.* Fluorescence Enhancement of Single V2 Centers in a 4H-SiC Cavity Antenna. *Nano Letters* **24**, 9289–9295 (2024).
18. Li, Q. *et al.* Room-temperature coherent manipulation of single-spin qubits in silicon carbide with a high readout contrast. *National Science Review* **9**, nwab122 (2022).
19. Son, N. T., Shafizadeh, D., Ohshima, T. & Ivanov, I. G. Modified divacancies in 4H-SiC. *Journal of Applied Physics* **132**, 025703 (2022).
20. Zhao, X., Liu, M. & Duan, C.-K. Analyzing Defect Complex Structures of PL6 in SiC: Insights from First-Principles Screening. *arXiv:2503.14170v1* (2025).
21. Chen, Y. *et al.* Atomic structure analysis of PL5 in silicon carbide with single-spin spectroscopy. *arXiv:2504.07558* (2025).
22. Jelezko, F. & Wrachtrup, J. Single defect centres in diamond: A review. *Physica Status Solidi (A) Applications and Materials Science* **203** (2006).
23. Doherty, M. W. *et al.* The nitrogen-vacancy colour centre in diamond. *Physics Reports* **528**, 1–45 (2013).
24. Childress, L. *et al.* Coherent Dynamics of Coupled Electron and Nuclear Spin Qubits in Diamond. *Science* **314**, 281–285 (2006).
25. Hu, H. *et al.* Strain Enhanced Spin Readout Contrast in Silicon Carbide Membranes. *arXiv:2506.00345* (2025).
26. Weitzel, C. E. *et al.* Silicon carbide high-power devices. *IEEE Transactions on Electron Devices* **43**, 1732–1741 (1996).
27. Sharmila, P., Supraja, G., Haripriya, D., Sivamani, C. & Narayana, A. L. Silicon carbide MOSFETs: A critical review of applications, technological advancements, and future perspectives. *Micro and Nanostuctures* **202**, 208126 (2025).
28. Hu, H. *et al.* Room-temperature waveguide integrated quantum register in a semiconductor photonic platform. *Nature Communications* **15**, 10256 (2024).
29. Zhou, J.-Y. *et al.* Plasmonic-Enhanced Bright Single Spin Defects in Silicon Carbide Membranes. *Nano Letters* **23**, 4334–4343 (2023).
30. Bao, T. *et al.* Deterministic and Scalable Coupling of Single 4H-SiC Spin Defects into Bullseye Cavities. *arXiv:2507.23258* (2025).
31. He, Z. X. *et al.* Robust single modified divacancy color centers in 4H-SiC under resonant excitation. *Nature Communications* **15**, 10146 (2024).
32. Falk, A. L. *et al.* Optical Polarization of Nuclear Spins in Silicon Carbide. *Physical Review Letters* **114** (2015).
33. Dutt, M. V. G. *et al.* Quantum Register Based on Individual Electronic and Nuclear Spin Qubits in Diamond. *Science* **316**, 1312–1316 (2007).
34. Bürgler, B. *et al.* All-optical nuclear quantum sensing using nitrogen-vacancy centers in diamond. *npj Quantum Information* **9**, 56 (2023).
35. Balasubramanian, G. *et al.* Nanoscale imaging magnetometry with diamond spins under ambient conditions. *Nature* **455**, 648–651 (2008).
36. Barry, J. F. *et al.* Sensitivity optimization for NV-diamond magnetometry. *Reviews of Modern Physics* **92**, 015004 (2020).
37. Metsch, M. H. *et al.* Initialization and Readout of Nuclear Spins via a Negatively Charged Silicon-Vacancy Center in Diamond. *Physical Review Letters* **122**, 190503 (2019).
38. Broadway, D. A. *et al.* High precision single qubit tuning via thermo-magnetic field control. *Applied Physics Letters* **112**, 103103 (2018).
39. Ziegler, J. F., Ziegler, M. D. & Biersack, J. P. SRIM - The stopping and range of ions in matter (2010). *Nuclear Instruments and Methods in Physics Research, Section B: Beam Interactions with Materials and Atoms* **268**, 1818–1823 (2010).

Supplementary materials to: RF-free driving of nuclear spins with color centers in silicon carbide

Raphael Wörnle,^{1,2,3,*} Jonathan Körber,^{1,2} Timo Steidl,^{1,2} Georgy V. Astakhov,⁴
Durga B. R. Dasari,^{1,2} Florian Kaiser,^{5,6} Vadim Vorobyov,^{1,2} and Jörg Wrachtrup^{1,2,3}

¹*3rd Institute of Physics, University of Stuttgart, Allmandring 13, 70569 Stuttgart, Germany.*

²*Center for Integrated Quantum Science and Technology, 70569 Stuttgart, Germany.*

³*Max Planck Institute for Solid State Research, Heisenbergstraße 1, 70569 Stuttgart, Germany.*

⁴*Helmholtz-Zentrum Dresden-Rossendorf, Institute of Ion Beam Physics and Materials Research, 01328 Dresden, Germany.*

⁵*Quantum Materials, Luxembourg Institute of Science and Technology (LIST),
28 Avenue des Hauts Fourneaux, 4362 Belval, Luxembourg.*

⁶*University of Luxembourg, 2 Avenue de l'Université, 4365 Belval, Luxembourg.*

(Dated: January 30, 2026)

S1. SINGLE DEFECT VERIFICATION

For the defects investigated in the main part, autocorrelation measurements were performed in the so-called Hanbury-Brown & Twiss interferometry experiment. The background-corrected measurements are shown for the PL6 center in Figure S1a and for the PL6 center with coupled nuclear spin in Figure S1b. Assuming a three level system for our defect [1], the theoretical second-order correlation measurement can be fitted using

$$g^{(2)}(\tau) = \frac{1}{N} \left(1 - (1 - a) \cdot e^{-\frac{\tau}{\tau_1}} + a \cdot e^{-\frac{\tau}{\tau_2}} \right) + \frac{N-1}{N} \quad \text{with} \quad g^{(2)}(\tau) \xrightarrow{\tau \rightarrow 0} 1 - \frac{1}{N}, \quad (1)$$

where a , τ_1 and τ_2 are the amplitude and the (anti-)bunching time constants and N the number of emitters [2]. The results in both cases yield values of $g^{(2)}(0) \ll 0.5$, which clearly confirms that each emitter is a single emitter.

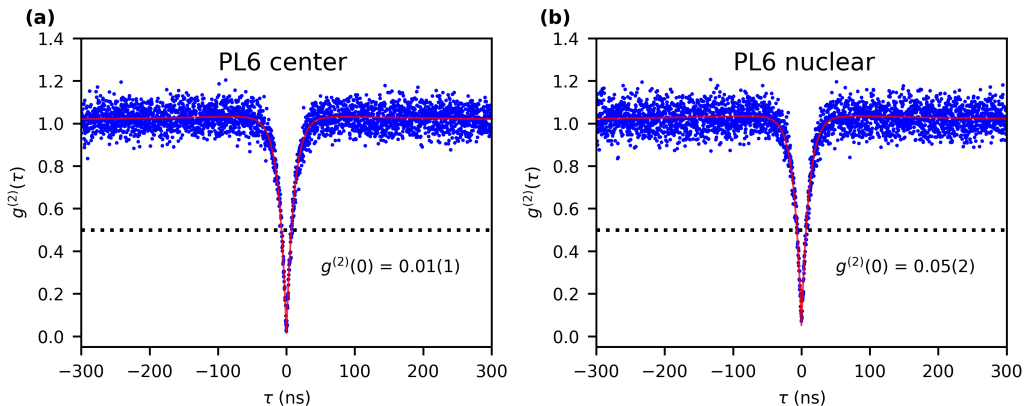


Figure S1: Autocorrelation measurements of PL6 centers. Background-corrected autocorrelation measurements measured at an excitation laser power of 100 μW for (a) a single PL6 center and (b) for the PL6 center coupled with a nearby nuclear spin. The fitted values for zero time delay yields a value of $g^{(2)}(0) = 0.01(1)$ for the PL6 center and $g^{(2)}(0) = 0.05(2)$ for the nuclear spin coupled PL6 center, both confirming the nature as single defects.

* E-Mail: raphael.woernle@pi3.uni-stuttgart.de

S2. NUCLEAR SPIN CONTROL

A. Nuclear spin identification

The nuclear spin defect shown in Figure 2b in the main text can also be experimentally classified to determine which type of nuclear spin it is. Hahn echo measurements are used for this purpose in a magnetic field of 145 G experimentally, which is illustrated in Figure S2. The relationship between the Larmor frequencies $f_L \propto \gamma_N \cdot B$ results in a gyromagnetic ratio of $\gamma_N = 10.88 \pm 0.12$ from the measurement, which corresponds relatively closely to the gyromagnetic ratio of $\gamma_{^{13}\text{C}} = 10.71$, therefore confirming the presence of a ^{13}C nuclear spin.

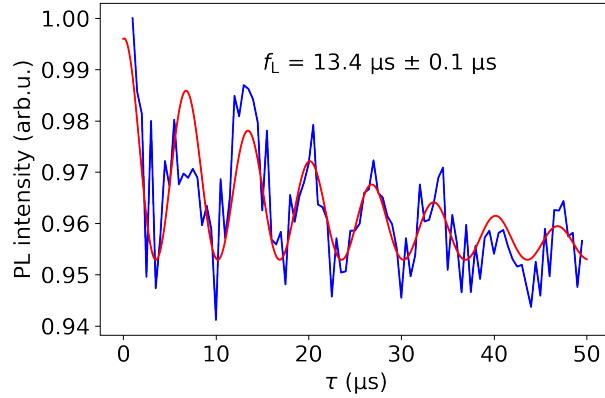


Figure S2: Nuclear spin identification. Hahn echo measurement on the PL6 with coupled nuclear spin in an external magnetic field of 145 G yielding a gyromagnetic ratio of $\gamma_N = 10.88 \pm 0.12$ matching the one for a ^{13}C nuclear spin.

This sequence can now be modified, resulting in the Hahn echo measurements of the nuclear spin in the main part in Figure 4.

B. Coupling strength

Exact control over the nuclear spin can only be achieved if the phase between the two nuclear spin states can also be manipulated. The exact strength of the coupling of the nuclear spin shown in Figure 2b in the main text can be determined using the following pulse sequence, shown in figure S3a. The idea and implementation were taken from [3]. For this purpose, the nuclear spin is initialized similarly as for the precession measurements.

Furthermore, a strong, non-selective π pulse excites both nuclear spin states; the subsequent waiting period before the second π pulse creates a relative phase on the nuclear spin state. Subsequently, a weak π pulse on the electron spin maps the system back onto the electron spin for read out, and the oscillations at the hyperfine coupling frequency ω_1 can be observed. In this case, a coupling strength of $\omega_1 = 2\pi \cdot 6.69(5)$ MHz is determined and shown in Figure S3b.

This sequence can now be modified, resulting in the Hahn echo measurements of the nuclear spin in the main part in Figure 4.

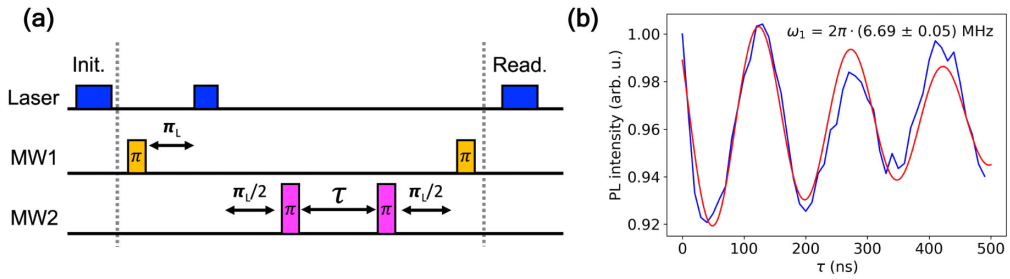


Figure S3: Nuclear spin coupling. (a) Measurement sequence for determining the exact coupling strength of the coupled nuclear spin. Sequence adapted from [3]. (b) Experimental result including damped cosine fit yielding a coupling strength of $\omega_1 = 2\pi \cdot 6.69(5) \text{ MHz}$.

C. Polarization

The sequence with the polarization step shown in Figure 2c in the main part can be extended by repeating the polarization step N times. The resonant driving of the nuclear spin polarizes it, thus improving the contrast. This is illustrated in Figure S4a in dependence of the number of polarization steps. It shows a saturation behavior whereby the contrast reaches almost twice the contrast of the CW-ODMR measurement seen in the main part in Figure 2b.

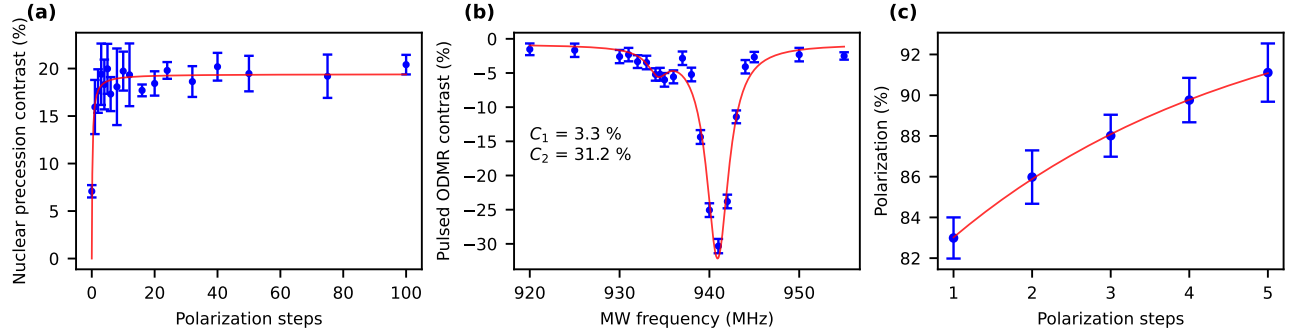


Figure S4: Polarization saturation study. (a) Saturation study of the measured contrast of the nuclear precession in dependence of the number of polarization steps with saturation fit $C = (C_{\text{Sat}} \cdot N) / (N + N_{\text{Sat}})$ yielding a saturation contrast of $19.4 \pm 0.7\%$. Error bars are determined by the fitted contrast and fit error of each measurement. (b) Pulsed ODMR measurement after previous polarization of nuclear spin yielding to a almost vanishing transition of the $| -1, \uparrow \rangle$ transition whereas the $| -1, \downarrow \rangle$ transition contrast is maximal. (c) Polarization study of ratios of the pulsed ODMR contrasts in dependence of the number of polarization steps with corresponding fit function yielding a saturation polarization behavior of $95.5 \pm 0.8\%$.

Additionally, high polarization can be achieved through repeating the shown polarization step in figure 2d in the main part multiple times, which has been shown to result in almost complete transition suppression. This is clearly achieved by performing $N = 5$ polarization steps and measuring pulsed ODMR. The result can be seen in Figure S4b, where a high degree of polarization is shown. In addition, a polarization study can be performed to determine the dependence of the polarization steps, as shown in Figure S4c. For this purpose, the polarization was determined from the ratio of the contrast of the two ODMR transitions. This results in a polarization of 95 % between the two states (in this case, $| -1, \uparrow \rangle$ and $| -1, \downarrow \rangle$). From this ratio, the effective zero-spin temperature can be determined using

$$p_{\uparrow} = p_{\downarrow} \cdot \exp \left(\frac{-\gamma_0 B}{k_B T} \right) \quad (2)$$

with $\omega_0 = \gamma_0 B$ as the Larmor precession frequency. In our case, the effective nuclear spin temperature gets calculated to $T_{\text{nucl}} = 400 \text{ nK}$. The idea was first shown by Dutt et al. (Suppl. S.2.4.2) [4].

S3. SECOND-ORDER PERTURBATION DERIVATION

In this section we derive the effective Hamiltonian acting on the nuclear spin within the $m_s = 0$ manifold of an $S = 1$ electronic spin coupled to a nuclear spin $I = 1/2$. The derivation follows the Van Vleck (Schrieffer–Wolff) perturbation procedure to second order, with all intermediate steps shown.

1. Full Hamiltonian and Hilbert-Space Partition

The complete spin Hamiltonian is

$$H = DS_z^2 + E(S_x^2 - S_y^2) + \gamma_e \mathbf{B} \cdot \mathbf{S} + \mathbf{S} \cdot \mathbf{A} \cdot \mathbf{I} - \gamma_l \mathbf{B} \cdot \mathbf{I}, \quad (3)$$

where $D \gg \gamma_e B, A_\perp$. We project the dynamics onto the two-dimensional subspace

$$\mathcal{H}_0 = \{|0,\uparrow\rangle, |0,\downarrow\rangle\},$$

while the electronic levels $|m_s = \pm 1\rangle$ form the excited subspace \mathcal{H}_1 .

We decompose:

$$H = H_0 + V, \quad (4)$$

where the unperturbed part is

$$H_0 = DS_z^2 + \gamma_e B_z S_z, \quad (5)$$

and the perturbation

$$V = \gamma_e (B_x S_x + B_y S_y) + \mathbf{S} \cdot \mathbf{A} \cdot \mathbf{I} - \gamma_l \mathbf{B} \cdot \mathbf{I}. \quad (6)$$

The unperturbed energies are

$$E_0 = 0, \quad (7)$$

$$E_+ = D + \gamma_e B_z, \quad (8)$$

$$E_- = D - \gamma_e B_z. \quad (9)$$

2. Matrix Elements of S_x and S_y

For an $S = 1$ spin:

$$\langle 0 | S_x | \pm 1 \rangle = \frac{1}{\sqrt{2}}, \quad (10)$$

$$\langle 0 | S_y | \pm 1 \rangle = \pm \frac{i}{\sqrt{2}}. \quad (11)$$

Define

$$B_\pm = B_x \pm iB_y.$$

Then

$$Z_\pm \equiv \langle 0 | \gamma_e (B_x S_x + B_y S_y) | \pm 1 \rangle = \frac{\gamma_e}{\sqrt{2}} B_\pm. \quad (12)$$

3. Off-Axis Hyperfine Terms

$$\mathbf{S} \cdot \mathbf{A} \cdot \mathbf{I} = A_{\parallel} S_z I_z + A_{\perp} (S_x I_x + S_y I_y).$$

Since $S_z |0\rangle = 0$, the term with A_{\parallel} vanishes in this subspace. Thus

$$V_{\text{hf},\perp} = A_{\perp} (S_x I_x + S_y I_y) = \frac{A_{\perp}}{2} (S_+ I_- + S_- I_+).$$

Using $\langle 0 | S_{\pm} | \pm 1 \rangle = 1/\sqrt{2}$:

$$H_+ = \langle 0 | V_{\text{hf},\perp} | +1 \rangle = \frac{A_{\perp}}{\sqrt{2}} I_-, \quad (13)$$

$$H_- = \langle 0 | V_{\text{hf},\perp} | -1 \rangle = \frac{A_{\perp}}{\sqrt{2}} I_+. \quad (14)$$

4. Van Vleck / Schrieffer–Wolff Formula

Projector P acts on \mathcal{H}_0 . The effective Hamiltonian up to second order is:

$$H_{\text{eff}} = PVP - \sum_{m=\pm 1} PV|m\rangle \frac{1}{E_m - E_0} \langle m| VP. \quad (15)$$

The first-order term gives the nuclear Zeeman interaction. The second-order sum contains the hyperfine-enhanced corrections.

5. Diagonal Second-Order Correction (ν_z)

Use:

$$H_{\pm} H_{\pm}^{\dagger} = \frac{A_{\perp}^2}{2} (I_x^2 + I_y^2) = \frac{A_{\perp}^2}{2} \cdot \frac{1}{4},$$

because $I = 1/2$.

Thus:

$$\nu_z = \frac{A_{\perp}^2}{2} \left(\frac{1}{E_+} + \frac{1}{E_-} \right) = A_{\perp}^2 \frac{E_+ + E_-}{2E_+ E_-}. \quad (16)$$

Using:

$$E_+ + E_- = 2D, \quad E_+ E_- = D^2 - (\gamma_e B_z)^2,$$

we obtain:

$$\nu_z = \frac{\gamma_e B_z A_{\perp}^2}{D^2 - (\gamma_e B_z)^2}. \quad (17)$$

6. Off-Diagonal Second-Order Term (ν_{\perp})

Mixed Zeeman–hyperfine processes produce:

$$H_{\text{eff}}^{(2)} \supset - \sum_{m=\pm 1} \frac{1}{E_m} (Z_m H_m^{\dagger} + H_m Z_m^{\dagger}). \quad (18)$$

1. Contribution from $m = +1$:

$$Z_+ H_+^\dagger = \frac{\gamma_e A_\perp}{2} B_+ I_+, \quad H_+ Z_+^\dagger = \frac{\gamma_e A_\perp}{2} B_- I_-.$$

2. Contribution from $m = -1$:

$$Z_- H_-^\dagger = \frac{\gamma_e A_\perp}{2} B_- I_-, \quad H_- Z_-^\dagger = \frac{\gamma_e A_\perp}{2} B_+ I_+.$$

Summing both:

$$\frac{\gamma_e A_\perp}{2} (B_+ I_+ + B_- I_-) \left(\frac{1}{E_+} + \frac{1}{E_-} \right). \quad (19)$$

Use identity:

$$B_+ I_+ + B_- I_- = 2(B_x I_x + B_y I_y) = 2B_\perp I_\perp \quad (\text{choosing } \parallel B_\perp).$$

Thus:

$$\nu_\perp = -\frac{2\gamma_e B_\perp A_\perp D}{D^2 - (\gamma_e B_z)^2}. \quad (20)$$

7. Final Effective Hamiltonian

Putting all the terms together:

$$H_{\text{eff}} = \frac{1}{2} \begin{pmatrix} \gamma_l B_z + \nu_z & \gamma_l B_\perp + \nu_\perp \\ \gamma_l B_\perp + \nu_\perp & -(\gamma_l B_z + \nu_z) \end{pmatrix}. \quad (21)$$

This is the effective nuclear-spin Hamiltonian used in the main text. It contains both hyperfine-enhanced longitudinal energy shifts and hyperfine-mediated transverse couplings arising from virtual electronic excitations.

S4. MAGNETIC FIELD OPTIMIZATION

In addition to the method described in the main part for aligning the magnet using nuclear spin precessions, there are three other methods, which are described below.

A. Optimization via count rate

The simplest and fastest method of aligning the magnetic field is by optimizing the count rate of a single PL6 center. For PL6 centers, the detected count rate is maximum when the magnetic field is aligned due to the inter system crossing rates of the Spin 1 system. The misalignment results in spin mixing, which partially pumps the system to the $m_s = 1$ or $m_s = -1$ state, causing the count rate to decrease. For the measurements, the lateral position of the magnet is swept and the count rate is measured for a fixed magnetic field. This is shown in Figure S5a for an applied external magnetic field. By fitting a 2D Gaussian function, the maximum count rate and thus the position with the best alignment can be found.

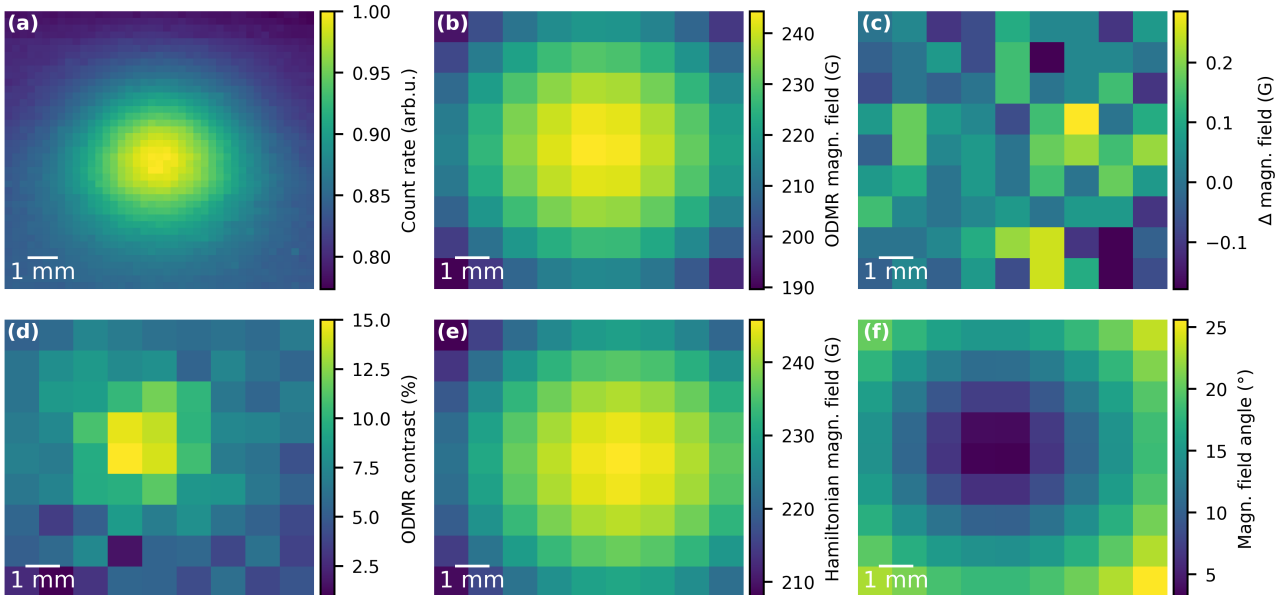


Figure S5: Magnetic field optimization. All measurements were done by sweeping the lateral position of the magnet in a fixed height above the sample. **(a)** Count rate of a single PL6 center in dependence of the external magnetic field. **(b)** Measured magnetic field via the $| -1 \rangle$ and $| +1 \rangle$ ODMR transitions. **(c)** Reproducibility study of the measurement in **(b)** by remeasuring the magnetic field and determining the differences compared to the first measurement to show a repetition and exact alignment of the magnet is given. **(d)** Contrast of the $| +1 \rangle$ transition in dependence of the magnetic field position. **(e)** & **(f)** Calculated external magnetic field strength and angle via the Hamiltonian.

B. Optimization via ODMR measurements

Another way to determine alignment is with ODMR measurements. When the magnetic field is aligned, the ODMR splitting between the two transitions is maximal, while it is reduced for deviations in alignment.

As with the count rate measurements, the lateral position of the magnet is swept, and for a single PL6 center, the ODMR transition $m_s = 0 \rightarrow m_s = \pm 1$ is measured and fitted with a 2D Gaussian function to find the ideal magnet position. From the difference between the two ODMR frequencies one can calculate the magnetic field strength which is depicted in Figure S5b. Furthermore, it is important to determine whether a reproducible magnet

position can be achieved to enable precise alignment. A repetition of the experiment in Figure S5b and subsequent comparison are shown in Figure S5c. It shows that only minimal differences in the magnetic field arise, which can be explained by the fitting uncertainty of the ODMR measurements. In addition, a clear dependence of the contrast in the ODMR measurement can be seen, which is shown in Figure S5d.

C. Optimization via Hamiltonian

With the ODMR frequencies already determined, the alignment can also be done using the Hamiltonian. This was already shown by Balasubramanian et al. in 2008 [5]. Here, only an abbreviated derivation is discussed.

In summary, from the reduced Hamiltonian to the electron spin from equation 1 in the main part, the magnetic field is characterized by the absolute strength B and the two polar and azimuthal angles Θ and φ by transforming the coordinates into polar coordinates. The position of the spin levels can be determined by solving the following equation for x

$$x^3 - \left(\frac{D^2}{3} + E^2 + \beta^2 \right) x - \frac{\beta^2}{2} \left(D \cos(2\Theta) + 2E \cos(2\varphi) \sin^2(\Theta) \right) - \frac{D}{6} \left(4E^2 + \beta^2 \right) + \frac{2D^3}{27} = 0 \quad (22)$$

with $\beta = \mu_B g B$. The relation

$$\Delta = D \cos(2\Theta) + 2E \cos(2\varphi) \sin^2(\Theta) \quad (23)$$

leads to

$$\beta^2 = \frac{1}{3} \left(\nu_1^2 + \nu_2^2 - \nu_1 \nu_2 - D^2 \right) - E^2 \quad (24)$$

and

$$\Delta = \frac{7D^3 + 2(\nu_1 + \nu_2)(2(\nu_1^2 + \nu_2^2) - 5\nu_1 \nu_2 - 9E^2) - 3D(\nu_1^2 + \nu_2^2 - \nu_1 \nu_2 + 9E^2)}{9(\nu_1^2 + \nu_2^2 - \nu_1 \nu_2 - D^2 - 3E^2)} \xrightarrow{D \gg E} \Delta \approx D \cos(2\theta) \quad (25)$$

for solutions for the magnetic field strength and the tilt angle and are illustrated in figure S5e & S5f.

S5. TOMOGRAPHY

A more detailed description of the tomographies of electron spin, nuclear spin and the coupled two-qubit system shown in Figure 5 in the main part follows here.

A. Electron spin

For the simple one-qubit case, electron spin tomography can be determined using Rabi oscillations. The system is initialized to the $m_s = 0$ state, in this case the transition $m_s = 0 \rightarrow m_s = -1$ is driven by a resonant microwave pulse, and finally, before the readout, one of three possible pulses is taken to measure the individual bases. No additional pulse is taken for the Z basis; for X and Y , a $\pi/2$ pulse is applied in the X - or Y -direction. This is achieved using the 90° phase shifter. The corresponding pulse sequence is shown schematically in Figure S6a.

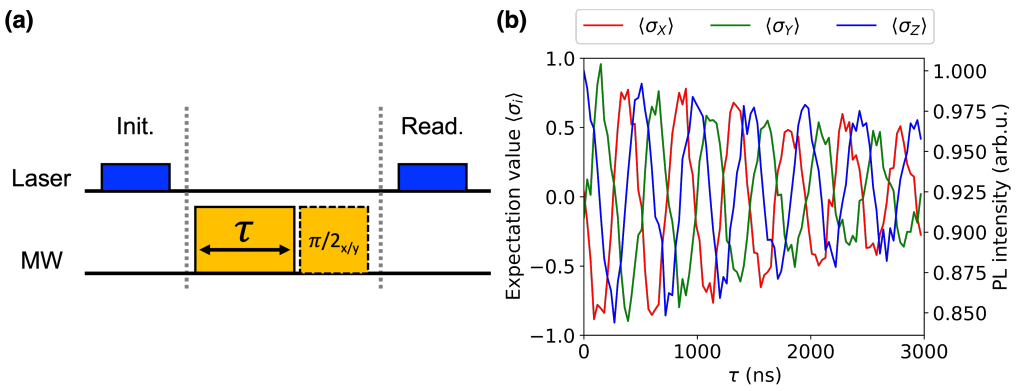


Figure S6: Electron spin tomography. (a) Measurement sequence for the electron spin tomography. For the Z basis, no additional pulse is applied whereas for the X and Y basis, a $\pi/2$ pulse in the corresponding direction is applied. (b) Experimental result for the electron spin tomography. The determined expectation values can be seen in Table S1.

Experimentally, the following three expectation values for X , Y , and Z are obtained, which are shown in Table S1. The absolute measured Rabi contrast is normalized to obtain an expectation value between -1 and 1. This is shown in Figure S6b. The first data point was used for the tomography because, as can be seen experimentally, the Rabi oscillations show exponential decay, and thus a false result would otherwise be formed.

Table S1: Electron spin tomography. Experimentally determined expectation values for the electron spin.

S_i	$\langle S_i \rangle$
Z	0.9353
X	0.0394
Y	-0.1555

Using these three expectation values, the density matrix for a one-qubit system can be determined. This works as follows:

$$\rho = \frac{1}{2} \left(I + \sum_i \langle S_i \rangle \sigma_i \right) \quad (26)$$

where I is the identity matrix and σ_i are the Pauli matrices.

$$I = \begin{pmatrix} 1 & 0 \\ 0 & 1 \end{pmatrix}, \quad X = \begin{pmatrix} 0 & 1 \\ 1 & 0 \end{pmatrix}, \quad Y = \begin{pmatrix} 0 & -i \\ i & 0 \end{pmatrix}, \quad Z = \begin{pmatrix} 1 & 0 \\ 0 & -1 \end{pmatrix} \quad (27)$$

Table S2: Nuclear spin tomography. Experimentally determined expectation values for the nuclear spin.

I	$\langle I \rangle$
Z	0.8574
X	0.1475
Y	0.1050

Using the experimental parameters, the density matrix can be reconstructed, and to determine the fidelity, the experimentally determined state is compared to the ideal state $|\Psi^+\rangle$ with

$$|\Psi^+\rangle = \begin{pmatrix} 1 & 0 \\ 0 & 0 \end{pmatrix} \quad (28)$$

and the fidelity F is determined as follows

$$F = \text{Tr} \left(\sqrt{\sqrt{\rho} \rho' \sqrt{\rho}} \right) \quad (29)$$

where ρ is the experimentally determined density matrix and ρ' the Bell state matrix.

B. Nuclear spin

For nuclear spin, tomography works in theory in exactly the same way as for electron spin. However, the nuclear spin cannot be read directly; therefore, as in all measurements, it is projected onto the electron spin to be read out.

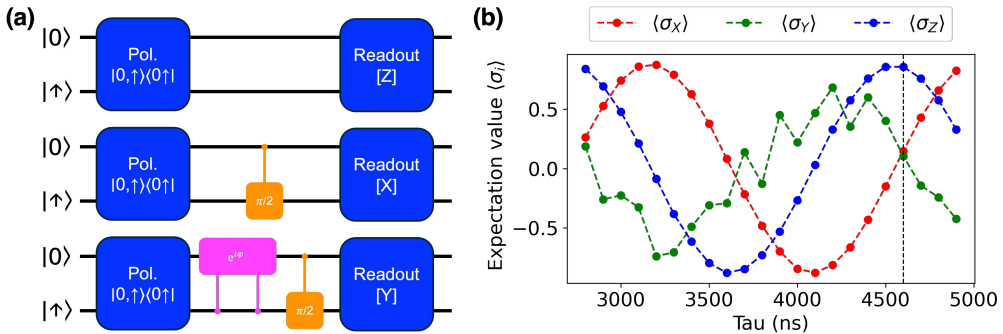


Figure S7: Nuclear spin tomography. (a) Measurement sequence for the nuclear spin tomography. For the Z basis, no additional pulse is applied. For the X basis, a waiting time of $\pi/2$ is applied. For the Y basis, additionally a phase is acquired using a MW 2π pulse with a subsequent waiting time to achieve the 90° rotation. (b) Experimental result for the nuclear spin tomography. The determined expectation values can be seen in Table S2.

For Z and X , tomography works similarly to electron spin. The measured value is used directly for the expectation value in Z , while a $\pi/2$ pulse in the x -direction is used for the expectation value in X . In this case, the $\pi/2$ pulse corresponds exactly to one waiting time of the nuclear spin precession by $\pi/2$. For the y -direction, it is not so trivial, since the method we described cannot control the precession in Y . However, this can be remedied by using the single pulse in X -direction and additionally adding a phase of the nuclear spin. Illustratively, the nuclear spin precesses when the electron spin is in the $m_s = 0$ state. If a 2π pulse is applied, the nuclear spin acquires a phase in the state $m_s = 1$, relatively to the $m_s = 0$ state. In our case, we apply two "fast" individual π pulses with a waiting time of $\tau_{\text{wait}} \approx 10$ ns between them. This value was chosen as a shorter waiting time would not be experimentally implementable and for longer waiting times the contrast of the nuclear precession would vanish due to decoherence. The schematic representation of the measurement of the three bases is shown in Figure S7a. The experimental results are as follows: the expected values for the nuclear spin in its three bases oscillate with its

precession frequency. For the tomography, the value at which the desired tomography state has a maximum Z value and minimal X and Y values is taken. In this example, this is the case at $\tau = 4600$ ns and is plotted in Figure S7b.

The exact values for the tomography are shown in Table S2. Using these values, as for the electron spin, the density matrix can be reconstructed and the fidelity determined, as already shown in the main section.

C. Two-qubit tomography

For the two-qubit tomography, the following change in the density matrix results compared to the one-qubit tomography

$$\rho = \frac{1}{4} \left(I \otimes I + \sum_{i,j} \langle S_i | I_j \rangle S_i \otimes I_j \right) \quad (30)$$

and the following Bell state, which should be created.

$$|\Psi\rangle = \frac{1}{2} \begin{pmatrix} 1 & 0 & 0 & 1 \\ 0 & 0 & 0 & 0 \\ 0 & 0 & 0 & 0 \\ 1 & 0 & 0 & 1 \end{pmatrix} \quad (31)$$

The entangled state is achieved, as shown in Figure 5c in the main part, by a global π pulse on the electron spin and half a Larmor precession. Global here means that the pulse is on both ODMR transitions, i.e. both spin up and spin down for the nuclear spin. For tomography, in contrast to the one-qubit case, not 3, but 9 measurements are required to measure all bases. This is achieved by combining the 3 bases for the nuclear spin with the three for the electron spin from Figures S6a and S7b. The nuclear spin is then projected onto the electron spin for readout. In this case, timing is extremely critical, especially since the microwave pulses are sometimes very short (30 ns for the Y rotation of the nuclear spin). This ensured that, for example, the waiting time for a nuclear spin precession was from the center of the microwave pulse to the center of the next pulse in order to achieve an exact rotation.

In addition, unlike the other measurements, a time-dependent measurement where one waiting time or pulse length is swept is not possible, as otherwise the state cannot be maintained and a mixed state would settle. Therefore, each measurement was performed with a fixed time and the expected value was determined using reference measurements. For the measurements, two reference measurements were taken, one with minimum and one with maximum contrast, to which all subsequent measurements were normalized.

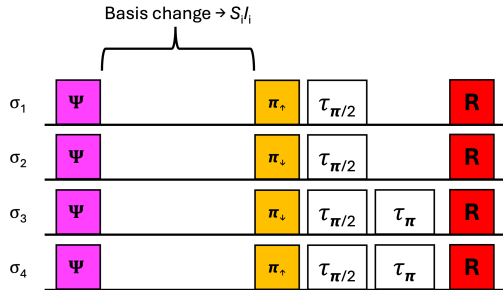


Figure S8: Tomography readout. Schematic representation of all four different readout possibilities to measure the expectation value needed for the two qubit tomography. The fourth readout was not performed due to the constraint that the sum of all σ_{i_l} equals to one.

For readout, the system was then brought into one of the two electronic states, $m_s = 0$ or $m_s = 1$, using pulse combinations. This is shown schematically in Figure S8. With these three measurements, the coefficients σ_{i_1} , σ_{i_2} , and σ_{i_3} can be determined, which are necessary for calculating the expectation values. The required fourth value can be determined using the relation $\sum_i \sigma_{i_l} = 2$. The 2 arises from the fact that, ideally, two measurements show maximum contrast, i.e., $\sigma_{i_l} = 1$, while two have minimum contrast, i.e., $\sigma_{i_l} = 0$, and thus the sum of these is 2. By halving the values, this can be normalized to 1 and using the relation $\langle \sigma_l \rangle = \sigma_{i_1} - \sigma_{i_2} - \sigma_{i_3} + \sigma_{i_4}$ the expectation value can be determined.

Table S3: Two-qubit tomography. Experimental results for the two-qubit tomography with all three experimentally determined parameters σ_{ij} used for calculating the expectation value $\langle S_i I_j \rangle$ for each basis.

S_i	I_j	σ_{ij_1}	σ_{ij_2}	σ_{ij_3}	$\langle S_i I_j \rangle$
Z	Z	0.982	0.018	0.058	0.924
X	X	0.891	0.140	0.009	0.851
Y	Y	-0.060	0.931	0.852	-0.783
X	Y	0.433	0.385	0.471	0.144
X	Z	0.347	0.496	0.541	-0.037
Y	X	0.392	0.487	0.477	0.036
Y	Z	0.486	0.526	0.473	0.001
Z	X	0.434	0.495	0.567	-0.062
Z	Y	0.551	0.460	0.443	0.097

The results of the measurements are shown in Table S3.

Analogous to the other two tomographies of the one qubit systems, the density matrix is reconstructed using the expected values and compared with the ideal Bell state, which was already described in the main text.

[1] J.-Y. Zhou, Q. Li, Z.-H. Hao, W.-X. Lin, Z.-X. He, R.-J. Liang, L. Guo, H. Li, L. You, J.-S. Tang, J.-S. Xu, C.-F. Li, and G.-C. Guo, Plasmonic-Enhanced Bright Single Spin Defects in Silicon Carbide Membranes, *Nano Letters* **23**, 4334 (2023).

[2] C. Kurtsiefer, S. Mayer, P. Zarda, and H. Weinfurter, Stable Solid-State Source of Single Photons, *Physical Review Letters* **85**, 290 (2000).

[3] L. I. Childress, *Coherent manipulation of single quantum systems in the solid state*, Ph.D. thesis, Harvard University, Cambridge (2007).

[4] M. V. G. Dutt, L. Childress, L. Jiang, E. Togan, J. Maze, F. Jelezko, A. S. Zibrov, P. R. Hemmer, and M. D. Lukin, Quantum Register Based on Individual Electronic and Nuclear Spin Qubits in Diamond, *Science* **316**, 1312 (2007).

[5] G. Balasubramanian, I. Y. Chan, R. Kolesov, M. Al-Hmoud, J. Tisler, C. Shin, C. Kim, A. Wojcik, P. R. Hemmer, A. Krueger, T. Hanke, A. Leitenstorfer, R. Bratschitsch, F. Jelezko, and J. Wrachtrup, Nanoscale imaging magnetometry with diamond spins under ambient conditions, *Nature* **455**, 648 (2008).